Applied Catalysis B: Environmental 129 (2013) 62–70

Contents lists available at SciVerse ScienceDirect

Applied Catalysis B: Environmental

journal homepage: www.elsevier.com/locate/apcatb

TiO_2 decoration of graphene layers for highly efficient photocatalyst: Impact of calcination at different gas atmosphere on photocatalytic efficiency

Adel A. Ismail[a,b,*], R.A. Geioushy[a], Houcine Bouzid[b], Saleh A. Al-Sayari[b], Ali Al-Hajry[b], Detlef W. Bahnemann[c]

[a] Nanostructured & Nanotechnology Division, Advanced Materials Department, Central Metallurgical R&D Institute, CMRDI, P.O. Box 87, Helwan 11421, Cairo, Egypt
[b] Advanced Materials and NanoResearch Centre, Najran University, P.O. Box 1988, Najran 11001, Saudi Arabia
[c] Photocatalysis and Nanotechnology Unit, Institut für Technische Chemie, Leibniz Universität Hannover, Callinstrasse 3, 30167 Hannover, Germany

ARTICLE INFO

Article history:
Received 28 June 2012
Received in revised form
12 September 2012
Accepted 13 September 2012
Available online 20 September 2012

Keywords:
TiO_2
Graphene
Layers
Calcination
Gas atmosphere
Photocatalysts

ABSTRACT

Graphene based two-dimensional carbon nanostructures serve as a support to disperse TiO_2 nanoparticles. Here, a facile decoration of graphene oxide (GO) and reduced graphene oxide (G) sheets with TiO_2 nanoparticles at different contents (1–10%) has been demonstrated. Then the as-prepared TiO_2–GO samples were heat treated at 450 °C under oxidizing (O_2), inert (N_2) and (Ar) and reducing (N_2/H_2) conditions to obtain multi-layers TiO_2–GO and TiO_2–G nanocomposites. The findings indicated that the lattice fringes of TiO_2 anatase exhibit the typical distances of (101) (3.54 Å) with high crystallinity. HRTEM images show the multi-layers TiO_2–G sheets with thicknesses ~2.4 nm. The newly prepared multi-layers TiO_2–GO and TiO_2–G nanocomposites have been compared with a commercial photocatalyst P-25 by the determination of their photocatalytic efficiencies for degradation of methylene blue. It can be observed that when TiO_2–GO calcining in N_2/H_2, the produced TiO_2–G shows a higher photocatalytic activity than those treated in N_2 and O_2. Also, the photocatalytic degradation rates of MB by TiO_2–G are faster 6 and 2 times than that by P25 and TiO_2–GO respectively, which is due to the better contact between G and TiO_2 and the more effective charge transfer from TiO_2 to G multi-layers. From the economic point of view, the consumed amount of TiO_2–G sheets in photocatalysis process is one fifth of commercial photocatalyst P-25 without loss of photocatalytic performance. Incorporation of TiO_2 nanoparticles onto multi-layers graphene sheets provide greater versatility in carrying out photocatalytic processes.

1. Introduction

Graphene offer new opportunities to develop nanocomposites with unusual electronic catalytic properties [1]. Graphene is an atomic sheet of sp^2-bonded carbon atoms that are arranged into a honeycomb structure [2]. Apart from its unique electronic properties, the two dimensional (2D) planar structure material has several other excellent attributes, such as the large theoretical specific surface area [3] and the high transparency due to its one-atom thickness [4]. Moreover, the surface properties of graphene could be adjusted via chemical modification, which facilitates its use in composite materials [5,6]. 2D carbon nanostructures such as graphene can potentially serve as a support material with which to anchor semiconductor particles and improve the performance of optoelectronic and energy conversion devices. The development of semiconductor–graphene or metal nanoparticle–graphene composites provides an important milestone to develop energy harvesting and conversion strategies [7]. Incorporation of catalyst particles onto an individual graphene or reduced graphene oxide (G) sheet with good distribution can provide greater versatility in carrying out selective catalytic or sensing processes [7–11]. TiO_2 has a large-band-gap semiconductors, and it is photocatalytically active under UV irradiation. TiO_2 is capable of interacting with graphene oxide via carboxylic acid functional groups [12,13]. Thus, the combination of TiO_2 and graphene is promising to simultaneously possess excellent adsorptivity, transparency, conductivity, and controllability, which could facilitate effective photodegradation of pollutants [14]. It is evident that the individual graphene sheets are coupled to TiO_2 nanoparticles. These TiO_2 nanoparticles are likely to interact through charge–transfer interaction with carboxylic acid functional groups or simple physisorption on the graphene oxide sheets [12]. The previous published papers reported the enhanced photocatalytic activity by GO–TiO_2 composite for water splitting, antibacterial application, and the degradation of organic pollutions [15–25]. Sun et al., [16] synthesized GO–TiO_2 nanocomposites by

* Corresponding author at: Nanostructured & Nanotechnology Division, Advanced Materials Department, Central Metallurgical R&D Institute, CMRDI, P.O. Box 87, Helwan 11421, Cairo, Egypt.
E-mail addresses: aismail@cmrdi.sci.eg, adelali11@yahoo.com (A.A. Ismail).

0926-3373/$ – see front matter © 2012 Elsevier B.V. All rights reserved.
http://dx.doi.org/10.1016/j.apcatb.2012.09.024

simply covering the functionalized graphene with P25 nanoparticles by heterogeneous coagulation. A sol–gel method to prepare GO–TiO_2 composites using tetrabutyl titanate and GO as the starting materials was demonstrated, and enhanced water photocatalytic splitting than that of P25 has been observed [17]. Liang et al. reported the synthesis of the high-quality GO–TiO_2 composites with better control in the size and morphology of TiO_2 nanoparticles [18]. Zhang et al. [14] prepared P25-graphene composite from P25 and GO in ethanol solution using a hydrothermal method, where GO was reduced to G during the hydrothermal process [20]. Also, GO–TiO_2 nanocomposites have been prepared using RF magnetron sputtering [21]. P25 TiO_2 materials are aggregated nanoparticles, it is difficult to anchor all P25 nanoparticles onto GO sheets very well. The well connection between TiO_2 and GO sheets is essential for the effective charge transfer and effective charge separation during the photocatalytic process.

On the other hand, a variation of the number of graphene layers may result in a striking change of their electronic properties [1]. Accordingly, it is very important to explore the production of graphene with number of layers in large quantities for their further fundamental studies and extensive applications. Wu et al. [26] have been succeeded to prepare a specific number of layers by selecting suitable starting graphite with high electrical conductivity $\sim 1 \times 10^3$ S/cm, which is ~3 orders of magnitude higher than that of individual GO reduced by hydrazine or sodium borohydride [27,28]. However, the prepared of high-quality TiO_2–graphene with a number of layers still remains a significant challenge for efficient photocatalysis applications. From this window, herein, we report a facile synthesis of multi-layers TiO_2–GO and TiO_2–G nanocomposites at different TiO_2 contents with highly dispersed onto GO and G sheet using titanium isopropoxide. The as-prepared TiO_2–GO were heat treated at 450 °C under oxidizing (oxygen), inert (N_2) and (argon) and reducing (N_2/H_2) conditions to obtain multi-layers TiO_2–GO and TiO_2–G nanocomposites. The present method offers several advantages over the previously reported ones, including (i) there was no an extra reducing agent, (ii) the in situ growth of TiO_2 leads to the formation of uniform nanoparticles on G sheets, and (iii) TiO_2–G with multi-layers have been prepared for highly diffusion and adsorption of dyes. To the best of our knowledge, the measured photodegradation rate of MB in the current work is found to be among the highest values reported up to now.

2. Experimental work

2.1.1. Materials

Graphite powder and sodium nitrate ($NaNO_3$, 98%) was obtained from Koch-Light Laboratories Ltd. Sulfuric acid (H_2SO_4 95–97%) and potassium permanganate ($KMnO_4$, 99.5%) and ethanol solution (99.9%) were purchased from Fluka and BDH Chemicals Ltd. Hydrogen peroxide solution (30%, w/v) pure reagent for analysis and titanium (IV) isopropoxide 97% ($C_{12}H_{28}O_4Ti$) were obtained from Aldrich.

2.1.2. Synthesis of TiO_2–GO and TiO_2–G

The synthesis of TiO_2–GO and TiO_2–G involve three key steps, (i) oxidation of the starting graphite to synthesize GO, (ii) impregnation of TiO_2 into GO sheets (iii) calcination of the as-prepared TiO_2–GO at 450 °C under oxidizing (O_2), inert (N_2) and (Ar), and reducing (N_2/H_2) conditions to obtain multi-layers TiO_2–GO and TiO_2–G nanocomposites.

2.2. Synthesis of graphene oxide (GO)

The graphene oxide (GO) was synthesized according to the modification of Hummers' methods [29] and the process was described previously [26]. Hummer method was used to prepare graphene oxide using 2 g graphite powder, 1 g sodium nitrate and 46 ml sulfuric acid were mixed and stirred at 0 °C for 15 min. 6 g potassium permanganate added slowly to the above solution and cooled for 15 min. Then the suspended solution was stirred for 1 h and 92 ml H_2O was added slowly for 10 min. the suspension was diluted by 280 ml of warm water. Finally, titrate the solution with 10 ml of H_2O_2 (30%). The resulting suspension was filtered, washed with water and dried at 60 °C for 24 h.

2.3. Synthesis of TiO_2–GO and TiO_2–G sheets nanocomposites

The presence of oxygen functional groups makes GO sheets strongly hydrophilic; stable aqueous dispersions consisting almost entirely of sheets with a thickness of 1 nm can be obtained by a mild ultrasonic treatment of graphite oxide in water [30]. 0.2 g of GO was prepared from graphite powder by Hummer method as shown above, was dispersed in a mixed solution of H_2O (10 ml) and ethanol (5 ml) in ultrasonic for 1 h. Then the calculated amount of titanium isopropoxide was added to graphene oxide suspension and ultrasonicated for another 1 h to obtain 1, 3, 5 and 10 wt% TiO_2–GO. The product was isolated by filtration and washed with distilled water and ethanol. The as-prepared 10 wt% TiO_2–GO sample were heat treated at 450 °C under oxidizing (oxygen), inert (N_2) and (argon) and reducing (N_2/H_2) conditions nanocomposites (labelled TiO_2–GO, TiO_2–GN, TiO_2–GA and TiO_2–G) to obtain TiO_2–GO and TiO_2–G sheets nanocomposites with TiO_2 anatase form as high photoactive phase.

2.3.1. Characterization

Transmission electron microscopy (TEM) was conducted at 200 kV with a JEOL JEM-2100F-UHR field-emission instrument equipped with a Gatan GIF 2001 energy filter and a 1k-CCD camera in order to obtain EEL spectra. Field emission-secondary electron microscope (FE-SEM) images were carried out with a FE scanning electron microanalyzer (JEOL-6300F, 5 kV). X-ray diffraction (XRD) data were acquired on a Bruker AXS D4 Endeavour X diffractometer using Cu $K\alpha_{1/2}$, $\lambda\alpha_1$ = 154.060 pm, $\lambda\alpha_2$ = 154.439 pm radiation. Raman spectroscopy was carried out using a WITEC CRM200 Raman system in the range from 500 to 2000 cm^{-1}. Infrared spectra were obtained on PerkinElmer Spectrun 100 FTIR-spectrometer in the range 350–5000 cm^{-1}. The samples were analyzed using the Thermo Scientific K-Alpha X-ray photoelectron spectrometer (Thermo Scientific, UK). The samples were mounted onto conductive tape and attached to a standard K-Alpha sample holder prior to introduction into the instrument. The XPS peaks for C1s and O1s were fitted to deconvolve the chemical states. A Shirley background was subtracted and peaks were fitted using Gaussian–Lorentzian shapes, where the Gaussian and Lorentzian functions were convolved to give the final peak envelope. Peaks were fitted using Thermo Scientific Avantage software. Photoluminescence (PL) spectra were measured by using RF-5301) fluorescence spectrophotometer with scan range from 220 to 900 nm and excitation wavelength at 280 nm. GO, 1 wt% TiO_2–GO, 10 wt% TiO_2–GO composites were dispersed in DI water for PL test.

2.4. Photocatalytic activity tests

The photocatalytic tests were performed in an aqueous solution using methylene blue (MB) (Aldrich, λ_{max} = 664 nm) as the probe molecule. A quartz photoreactor was filled with 200 cm^3

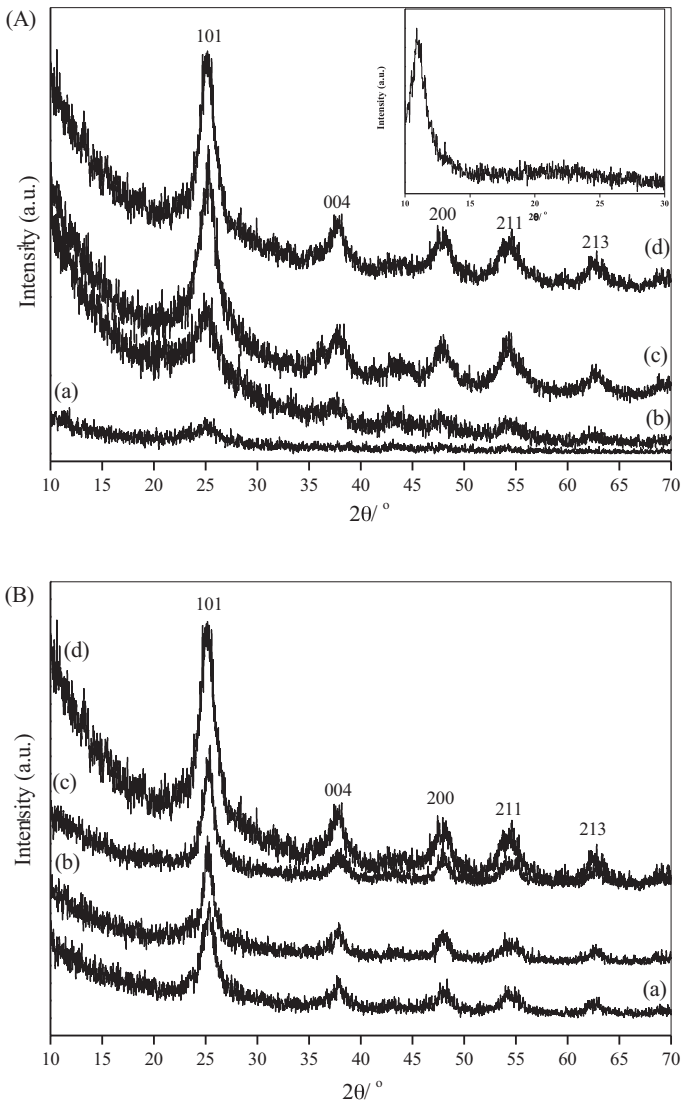

Fig. 1. (A) XRD patterns of TiO_2–GO nanocomposites at different TiO_2 content 1 wt% (a), 3 wt% (b), 5 wt% (c) and 10 wt% (d), inset (A) XRD patterns of GO; (B) XRD patterns of 10 wt% TiO_2–GO heat treated at 450 °C under inert Ar (a), N_2 (b), reducing (N_2/H_2) (c) and oxidizing (O_2) (d).

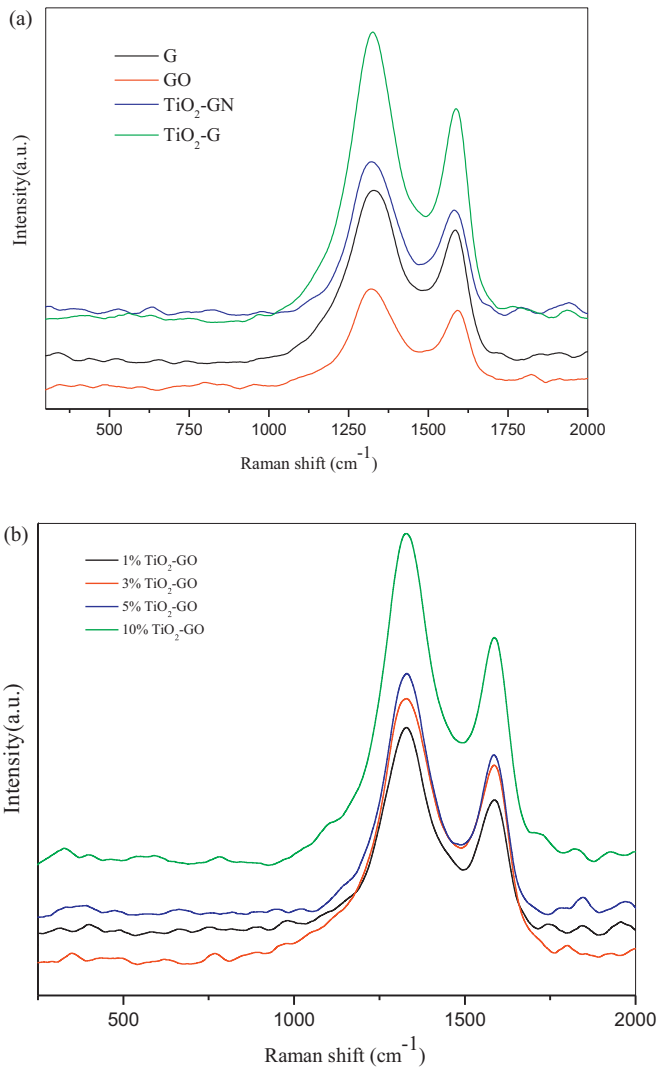

Fig. 2. Raman spectra of GO and G and TiO_2–GN and TiO_2–G composites (a). Raman spectra TiO_2–GO nanocomposites at different TiO_2 content 1 wt%, 3 wt%, 5 wt% and 10 wt% (b).

aqueous solution of MB at a concentration of 10 ppm. UV irradiation was performed by a 150 W medium pressure xenon lamp (Osram) immersed in a quartz jacket and equipped with a cooling tube. The lamp was switched on 30 min prior to the start of the reaction to stabilize the power of its emission and the reactor was cooled by circulation of H_2O. The temperature of the cooling water was stabilized to perform the reactions at 25 °C. For visible light test, the reactor was illuminated by a 1000 W halogen lamp. The distance between the sample and the halogen lamp was set at 25 cm. Photooxidation reactions were carried out suspending 0.5 g/l of the prepared photocatalysts with oxygen being purged through the reaction vessel continuously. The suspensions were sonicated at the desired aqueous solution of MB before the experiment was started and they were stirred in the dark for 30 min to reach the adsorption equilibrium prior to irradiation. The concentration of the substrate after equilibration was measured and taken as the initial concentration (C_0) to discount the adsorption in the dark. MB samples were withdrawn at regular intervals (C) from the upper part of the reactor with the catalyst being removed from the liquid phase by filtration through nylon syringe filters (pore size: 0.45 μm). The concentration of MB (C) is proportional to the maximum absorbance at 644 nm (A). Thereby we analyzed the change of concentration (C/C_0) from the variation of absorbance (A/A_0), where C_0 and A_0 are the initial concentration and absorbance of MB, respectively. The photodegradation rate was determined by measuring the MB remained in the aqueous solution through 3 h of illumination using JASCO V-570 UV–vis spectrophotometer. Total Organic Carbon (TOC) analysis of the samples were measured using Phoenix 8000 UV-persulfate TOC Analyzer.

3. Results and discussions

3.1. Structural investigations

GO based 2D carbon nanostructures serve as a support to disperse TiO_2 nanoparticles. TiO_2 is dispersed into the GO sheets and then the prepared materials were calcined at 450 °C under oxidizing (oxygen), inert (N_2) and (Argon) and reducing (N_2/H_2) conditions. The X-ray diffraction (XRD) patterns of GO (inset Fig. 1A) and TiO_2–GO nanocomposites at different TiO_2 content 1 wt%, 3 wt%, 5 wt% and 10 wt% were shown in Fig. 1A. Fig. 1A inset revealed that a diffraction pattern of GO has a peak centered at $2\theta = 11.8°$, corresponding to the [0 0 1] interlayer spacing of 7.43 Å [31]. This illustrates that most of the natural graphite was oxidized into GO

[32]. The XRD analysis confirms that TiO_2 has been effectively intercalated into the GO stacks. It is found that though the TiO_2 content increased, all samples, show a similar crystal composition. However, the intensity of the diffraction peaks for the composites show increase as the TiO_2 content increased (Fig. 1A). In order to confirm the bulk composition for each sample, the XRD patterns were compared with the JCPDS-ICDD standards for anatase (21–1272). The diffractograms for TiO_2 are essentially equivalent, exhibiting peaks at 25.4°, 36.4°, 48.1°, 54.2° and 62.8° that are consistent with the (1 0 1), (0 0 4), (2 0 0), (2 1 1) and (2 1 3) planes associated with tetragonal anatase. The Rietveld refinements of the diffraction patterns show that only anatase was formed and no reflections of any other phases of TiO_2. However, the [0 0 1] reflections of GO are not observed in the XRD pattern of TiO_2–GO because the regular stack of GO was destroyed by the intercalation of TiO_2 [17,28,33]. The average crystal size calculated by applying the Scherrer formula on the anatase (1 0 1) diffraction peaks is ranged 5–15 nm for these samples. Fig. 1B shows XRD patterns of 10 wt% TiO_2–GO heat treated at 450 °C under inert Ar, N_2, reducing (N_2/H_2) and oxidizing (O_2), suggesting that calcination at different gases did not affect the structure of anatase phase. The existence of GO in the TiO_2–GO nanosheets is also proved in their Raman spectra (Fig. 2). The results revealed that there are two mean peak at around 1330 cm^{-1} and 1589 cm^{-1} for all prepared samples GO and G and TiO_2–GN and TiO_2–G composites (Fig. 2a) and TiO_2–GO nanocomposites at different TiO_2 content 1 wt%, 3 wt%, 5 wt% and 10 wt% (Fig. 2b). The peak at around 1589 cm^{-1} is characteristic for graphitic sheets and we were able to record well defined G-band which confirms the presence of sp^2 carbon-type structure. The D-band at around 1330 cm^{-1} can be attributed to the presence of defects within the hexagonal graphitic structure. The peaks at about 1330 cm^{-1} (D band) and 1589 cm^{-1} (G band) are attributed to the graphite substrate [34]. For comparison with that of GO, a decreased D/G intensity ratio is observed, suggesting that the defects in G are increased after the reduction of GO [35]. And it is obvious that the D/G intensity ratio decreased along with the increasing of G content in the TiO_2–G composites, proving the existence of G in the TiO_2–G composites.

FE-SEM images of TiO_2–GO at 1, 3, 5 and 10 wt% TiO_2 is shown in Fig. 3a–d, respectively. The TiO_2–GO at low TiO_2 contents presents the sheet-like structure with the large thickness, smooth surface, and wrinkled edge. At high TiO_2 content, it is uniformly decorated and firmly anchored on the wrinkled graphene layers with a high density (Fig. 3d). The pleats structure of the GO may favor to hinder the TiO_2 from agglomeration and enable their good distribution on the graphene. Interestingly, after H_2 reduction, a significant change in morphology can be observed from Fig. 3e and its sheets display layered structures and become very thin with ordered platelets. Also, FE-SEM images of TiO_2–GO and TiO_2–G demonstrate that the 2-D molecular sheet was well preserved after calcination at 450 °C under O_2, H_2 and N_2 (Fig. 3d–f). HRTEM images show the multi-layers 10 wt% TiO_2–G sheets (Fig. 4). The maximum thicknesses of multi-layers graphenes derived from HRTEM images are 2.4 nm. According to the measured thicknesses of multi-layers G containing 10 wt%TiO_2, the interlayer spacing can be calculated to be in the range of 0.4–0.5 nm. Obviously, this value is much larger than that of graphite, normally 0.335 nm. As a consequence, the real thickness of the obtained graphene should be the sum of the observed thickness from HRTEM and the thickness increase caused by the presence of epoxy and hydroxyl groups on both sides of the surface [26]. Both the edge of graphene and TiO_2 nanoparticle are clearly observable in the higher magnification image of Fig. 4a. The lattice fringes of TiO_2 exhibit the typical distances of (1 0 1) (3.54 Å) (Fig. 4b). The clear lattice of TiO_2 anatase indicates that the TiO_2 is of high crystallinity. The energy-dispersive X-ray (EDX) spectrum of TiO_2–GO and TiO_2–G (data not shown) exhibited the presence of C, O, and Ti elements, further confirming the formation of TiO_2–GO composite.

X-ray photoelectron spectroscopy (XPS) was performed on TiO_2–GO and TiO_2–G samples (Fig. 5). The full-scale XPS spectra (Fig. 5a) show the existence of C, O, and Ti in TiO_2–G. Two peaks centered at 459.4 and 465.1 eV can be seen from the Ti 2p spectrum (Fig. 5b) that are assigned to Ti $2p_{1/2}$ and Ti $2p_{3/2}$, respectively, in good agreement with the binding energy values of Ti^{4+} in pure anatase [36]. The core-level XPS signals of C 1s shown in Fig. 5c were deconvoluted into three components. For the TiO_2–G sample, the main peak centered at about 284.6 eV originated from the graphitic sp^2 carbon atoms. The binding energies located at 286.7 eV and 287.9 eV are due to carbon atoms connecting with oxygenate groups, such as C—O and O—C=O [37]. The small peaks related to oxygenate groups indicate the presence of residual oxygenate groups on the TiO_2–G sample. The weaker peaks due to oxygenate groups suggest a considerable de-oxygenation and the formation of TiO_2–G [38]. A small amount of residual oxygenate groups on GO–TiO_2 are believed to be favorable for maintaining a good dispersion of the composite nanosheets. The respective O:C atomic ratios for TiO_2–GO and TiO_2–G are 0.54 and 0.22 and Ti:C atomic ratios for TiO_2–GO and TiO_2–G are 0.06 and 0.05, respectively. It is clear that the photocatalytic application of TiO_2–G resulted in an evident decrease in oxygen content, which will further enhance the conductivity of GO sheets as you see below.

Fig. 5d shows the Fourier transform infrared (FTIR) spectra of 10 wt% TiO_2–GO (a), GO (b), 10 wt% TiO_2–G (c), and G (d) in the range of 4000–450 cm^{-1}. GO (Fig. 6b), the absorption due to C=O stretching of COOH groups situated at the edge of GO sheets was observed at about 1739 cm^{-1}. The peak at around 1617 cm^{-1} was assigned to the O—H bending. The absorption peaks at 1229 cm^{-1} and 1050 cm^{-1} were attributed to the tertiary C—OH and C—O stretching mode, respectively. While in G curve (Fig. 6d), the absorption peaks for the O—H bending, tertiary C—OH and C—O stretching were absent. The C=O stretching (1726 cm^{-1}) decreased a lot in intensity and the absorption band that appeared at ca. 1600 cm^{-1} clearly showed the skeletal vibration of the graphene sheets [39]. After the introduction of 10 wt% TiO_2 to GO and G as shown in curves Fig. 6a and c, the absorption peak corresponding to Ti—O—Ti of TiO_2 shifted to higher wavenumber than pure TiO_2 (data not shown). The shift was attributed to the combination of the vibration of Ti—O—Ti and Ti—O—C bonds [40]. The FTIR results confirmed the formation of Ti—O—C bonds between TiO_2 and either GO and G and also GO sheets were reduced to G with a small amount of residual carboxylic acid groups.

3.2. Photocatalytic degradation of MB

The photocatalytic activities of TiO_2 decorated with GO at different contents TiO_2 (1–10 wt%) has been assessed by the photodegradation of aqueous solutions of methylene blue [10 ppm] as model reaction under UV light and quantitatively compared with P 25. Fig. 6a shows UV–vis absorption spectra recorded during the photocatalytic decomposition of MB solution (aqueous, O_2 saturated) at UV irradiated 10 wt%TiO_2–G composites. It is obvious that, the strong absorption bands of MB those are located at $\lambda = 291$ nm and $\lambda = 664$ nm steadily decrease upon increasing irradiation times. The absorption bands of MB has disappeared after photocatalytic degradation by TiO_2–G composites indicating the photocatalytic degradation of the MB in about 8 min. The disappearance of the absorption bands of MB at 664 nm suggests that MB is well-absorbed by multi-layers G sheets. Because of similar conjugated aromatic cycles, the interaction of π-conjugated and the ion-dipole interactions between G and MB will take place, which leads to the adsorption of MB by G sheets.

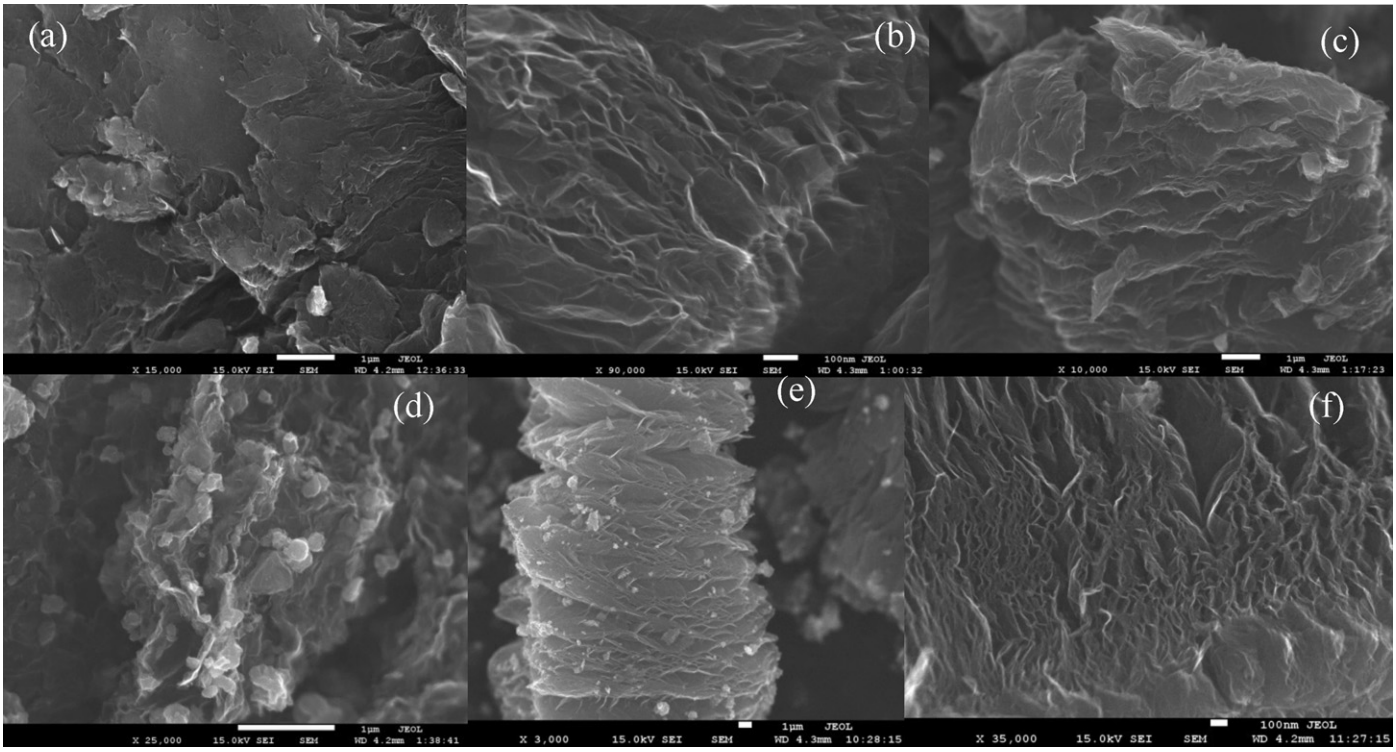

Fig. 3. FE-SEM images of TiO_2–GO nanocomposites at different TiO_2 content 1 wt% (a), 3 wt% (b), 5 wt% (c) and 10 wt% TiO_2–GO heat treated at 450 °C under reducing (N_2/H_2) (e), Nitrogen (f).

However, adsorption was not the only influential factor. First, without irradiation, the dye solution achieved adsorption equilibrium after 10 min, and more than 50% of the initial dye molecules still remained in the solution after 30 minute using 10 wt%TiO_2–GO (Supporting Information Figure S1)

Fig. 6b shows the photogeradation of MB using TiO_2 (1–10 wt%)–GO as a photocatalysts. The finding indicated that the photodegradation rate is increased from 31 to 100% with increasing TiO_2 content up to 10% and these results were confirmed by TOC measurements. The enhancement of the photocatalytic activity could be attributed to the excellent electronic conductivity and large specific surface area of TiO_2–GO, resulting that the photoinduced electrons transport to the surface of the composites more easily, thus inhibiting the recombination between photoinduced electrons and holes. It can be seen that the surface areas of the samples increased from 29.03 to 192 m^2/g with increasing TiO_2 contents from 0 to 10 wt%. The surface area of 10 wt%TiO_2–GO is higher 4 times than that Degussa P-25 (45 m^2/g). The large surface area can adsorb significant amounts of water and hydroxyl groups [41]. Interestingly, MB can be well adsorbed by G and GO sheets, which is beneficial to the enhanced photocatalytic activity of either TiO_2–GO or TiO_2–G nanocomposites. Upon excitation by UV light, electron–hole pairs are generated within TiO_2. As the electrons are scavenged by dissolved oxygen or the accumulated electrons serve to interact with the GO sheets in order to reduce certain functional groups, the holes participate in the generation of •OH

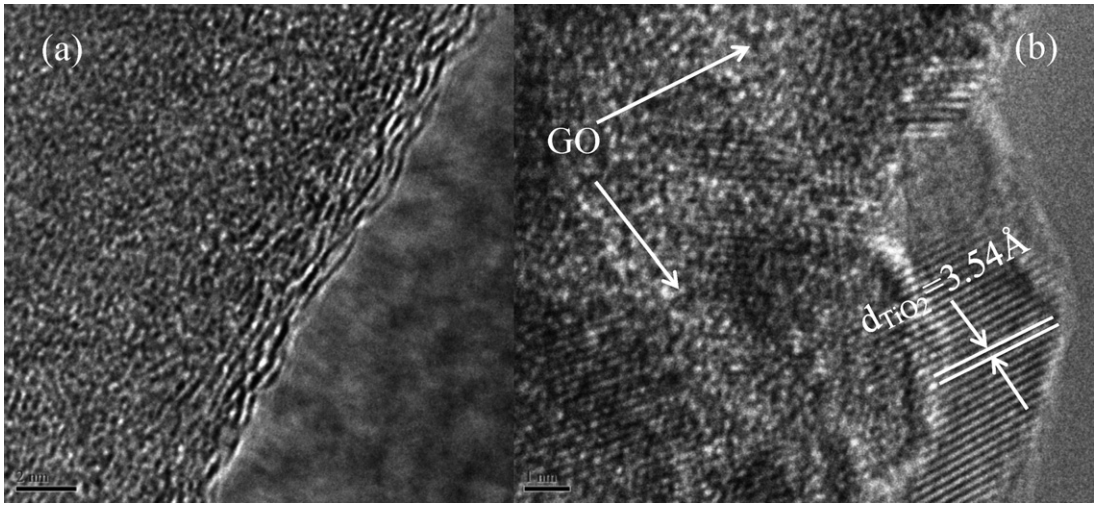

Fig. 4. HRTEM images of 10 wt% TiO_2–G with triple-layers graphene sheets and folded edges obtained by chemical exfoliation (a). HRTEM image of 10 wt% TiO_2–GO; the lattice fringes exhibit the typical distances TiO_2 (1 0 1) (3.54 Å) (b).

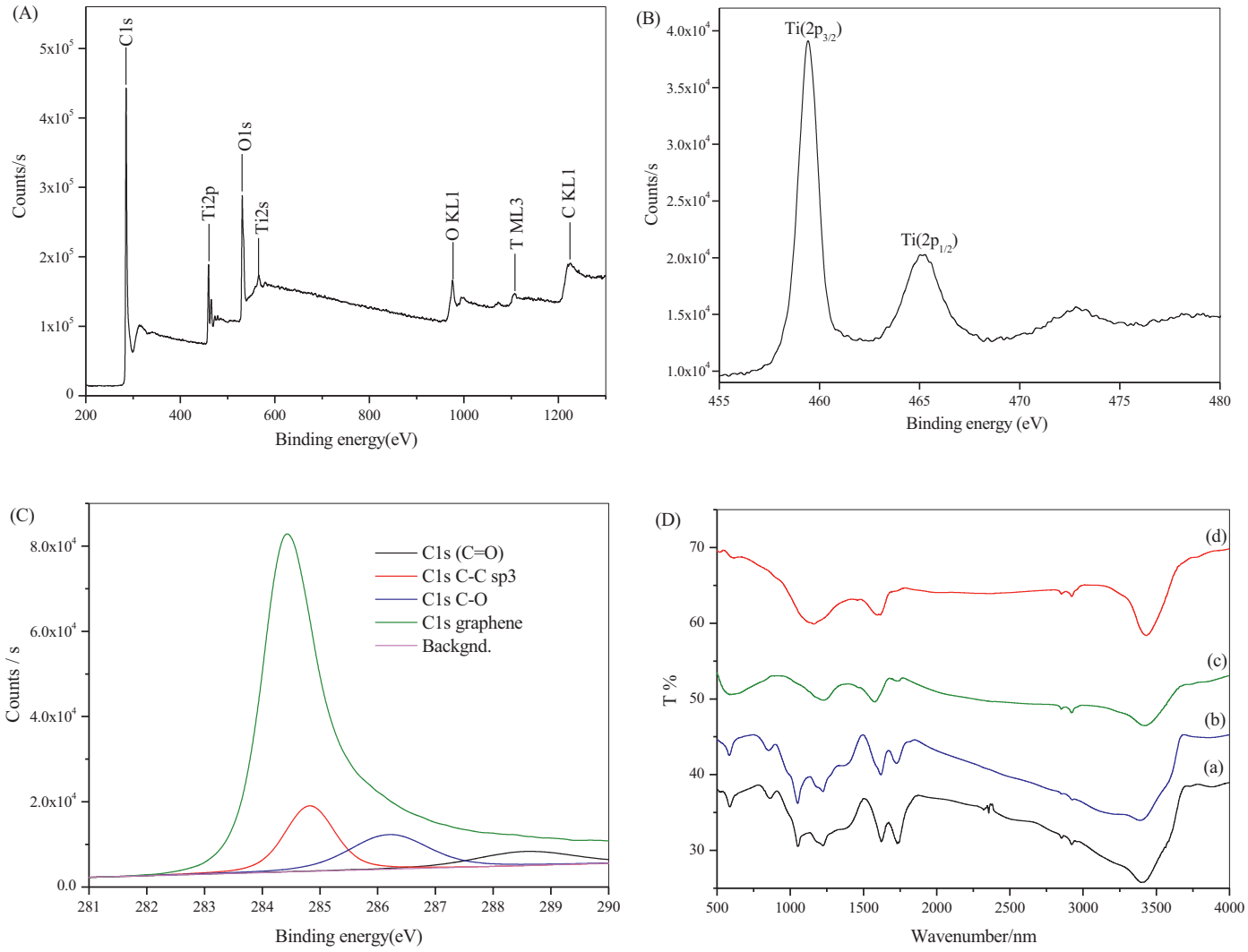

Fig. 5. (A) XPS survey spectra of TiO_2–G. Core level XPS spectra of (B) Ti 2p. C 1s XPS spectra of (C) TiO_2–G, (D) FTIR spectra of GO (a), 10%TiO_2–GO (b), 10%TiO_2–G (c), and G (d) in the range of 4000–450 cm^{-1}.

radicals that oxidize MB (Scheme 1). The holes can either directly oxidize the organic substrate or can transfer to the adsorbed water to form hydroxyl radicals [42]. Work function of GO is in the range of 4.42–4.5 eV [12,43]. It signifies possible electrons moving from conduction band of TiO_2 to GO as shown in the following equations.

$$TiO_2 + h\nu \rightarrow TiO_2(e + h)$$

$$TiO_2(e) + O_2 + GO \rightarrow TiO_2 + O_2 + GO(e)$$

$$TiO_2(h) + OH^- \rightarrow TiO_2 + {}^{\bullet}OH$$

$$TiO_2(h) + {}^{\bullet}OH + MB \rightarrow \text{degradation products}$$

The efficient charge separation and transfer are crucial for the enhanced photocatalytic activity of TiO_2–GO. The photoluminescence (PL) spectra of GO, 1%TiO_2–GO, 10%TiO_2–GO composites were investigated and excited at 280 nm (Fig. 7b). The GO show a PL emission band at 566 nm, after combined with TiO_2, the PL spectrum of 5%TiO_2–GO is slightly raised and the PL spectra is continuously increased. This is because TiO_2 nanoparticles are anchored with the GO sheets. The photogenerated electron can transport along the GO sheets and then react with the absorbed O_2 to form •OH for the further photocatalytic degradation of MB. The schematic illustration of the charge transfer and enhanced photocatalytic activity by TiO_2–GO is summarized in Scheme 1.

In order to investigate the effect of calcination atmosphere on the photocatalytic activity of the TiO_2–GO composites, The photocatalytic activities for the samples calcined at 450 °C under oxidizing (O_2), inert (N_2) and (argon) and reducing (N_2/H_2) conditions to obtain multi-layers TiO_2–GO and TiO_2–G sheets are shown in Fig. 7a. It can be observed that when calcining in N_2/H_2, the produced TiO_2–G shows a higher photocatalytic activity than those treated in N_2 and O_2. When calcining in O_2, free carbon in the surface of TiO_2 prefers to react with O_2, while in a N_2 atmosphere it favors oxygen in the lattice of TiO_2, leading to the formation of oxygen vacancies [44]. These oxygen vacancies can act as electron traps. Thus, in general, TiO_2–GO samples calcined in a N_2 atmosphere show a higher photocatalytic performance than those calcined in O_2 (Fig. 7a). Also, the calcination under N_2/H_2 confirmed the TiO_2–G was formed with decreasing in oxygen content, which will further enhance the conductivity of GO sheets. According XPS results and to the mechanism by Hoffman et al. [45] the higher conductivity leads to more effective charge separation and more effective antirecombination during photocatalytic process. The decay of MB during the initial period of UV excitation was fitted to pseudo-first-order kinetics. The rate constants k (min^{-1}) for MB

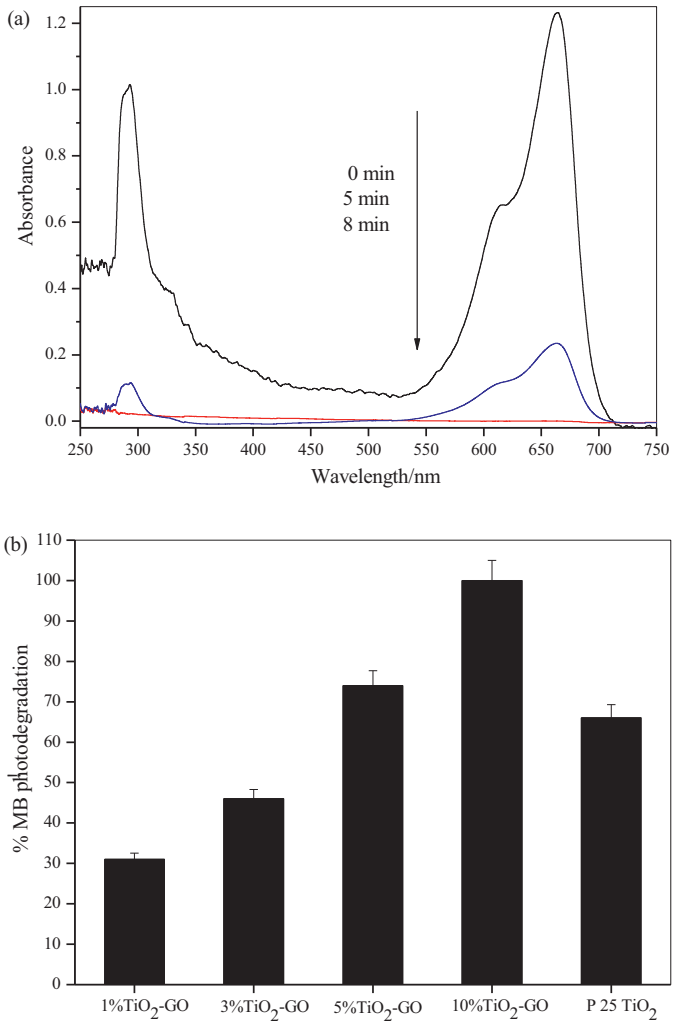

Fig. 6. (a) Absorbance vs. wavelength as a function of illumination time for the photocatalytic degradation of MB on 10%TiO_2–GO; (b) MB degradation rate (%) of TiO_2–GO nanocomposites at different TiO_2 content 1%, 3%, 5% and 10 wt% and commercial photocatalysts P-25 Degussa under UV light (λ = 365 nm) for 30 min (MB concentration [10 ppm], photocatalyst loading, 0.5 g/l volume of MB = 100 ml).

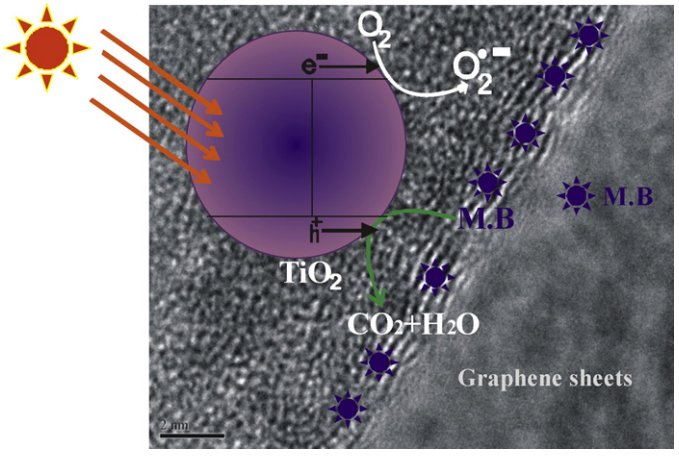

Scheme 1. Schematic structure of multi-layers TiO_2–G nanocomposites and tentative processes of the photodegradation of methylene blue (MB). The carbon platform plays important roles during the photodegradation of MB (i) increase catalyst adsorptivity; MB molecules could transfer from the solution to the multi-layers TiO_2–G; (ii) absorption of UV light by the semiconducting nanoparticle promotes an electron from the valence band to the conduction band; (iii) Suppress charge recombination. Graphene could act as an acceptor of the photogenerated electrons by TiO_2, and therefore, an effective charge separation can be achieved.

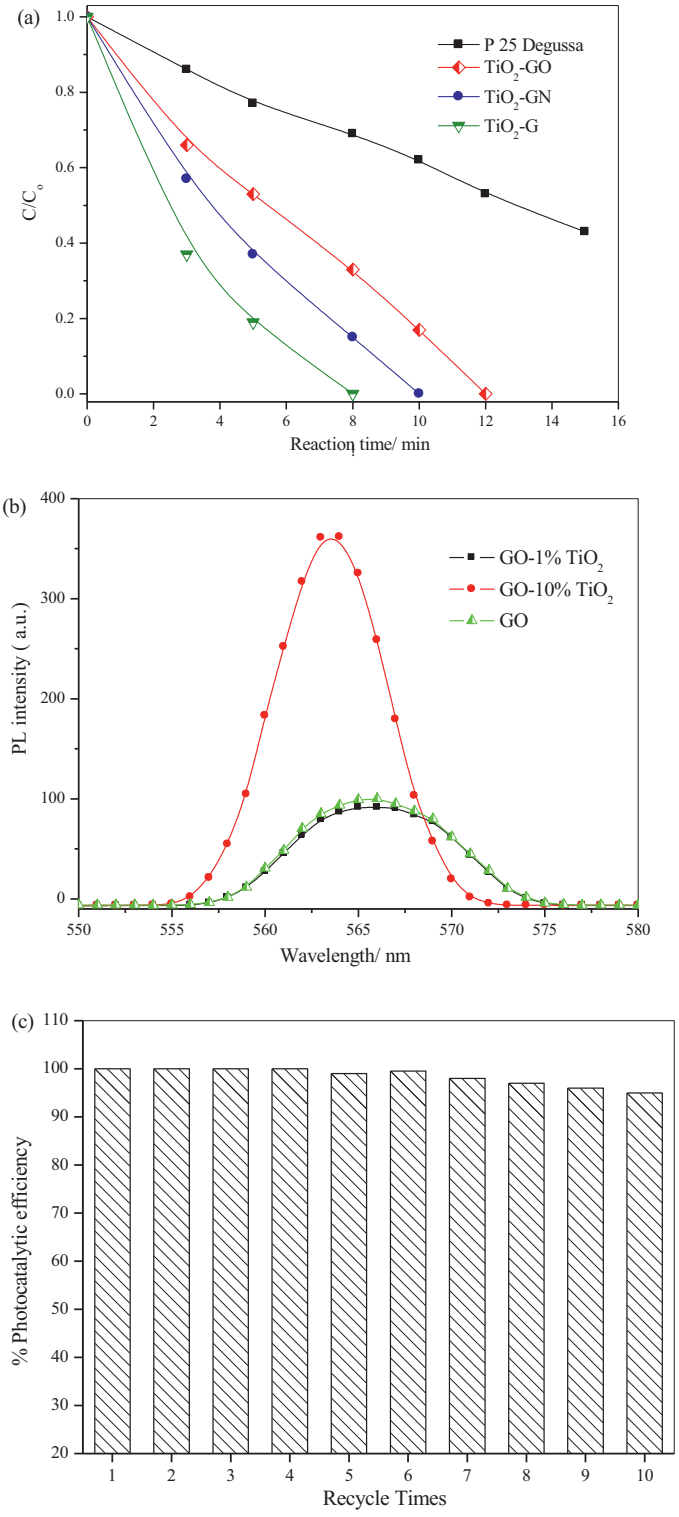

Fig. 7. (a) Photocatalytic degradation of MB in aqueous solution over 10 wt% TiO_2–GO heat treated at 450 °C under inert (N_2)TiO_2–GN, reducing (N_2/H_2) TiO_2–G and oxidizing (O_2) TiO_2–GO samples and Degussa P-25 under UV lights (MB concentration [10 ppm], photocatalyst loading, 0.5 g/l volume of MB = 100 ml); (b) photoluminescence spectra of GO, 1%TiO_2–GO, 10%TiO_2–GO composites (b), recycling test over 10%TiO_2–G for photocatalytic degradation of MB [10 ppm] repetitively for 10 times (UV light (λ = 365 nm) for 10 min, photocatalyst loading, 0.5 g/l, volume of MB = 100 ml).

degradation constants using P25, TiO_2–GO, TiO_2–GN and TiO_2–G composites are 0.054, 0.168, 0.236, and 0.332, respectively. It is apparent that the photocatalytic degradation rates of MB by TiO_2–G are faster 6 and 2 times than that by P25 and TiO_2–GO respectively, which is due to the better contact between G and TiO_2 and the more effective charge transfer from TiO_2 to G sheets. In addition to the improved charge separation, the G sheets can overcome the mass transfer limitation by increasing the availability of MB near the photocatalyst surface. The faster rate of MB photodegradation observed with TiO_2–G points out the additional benefit of concentrating the organics near the photocatalyst surface.

We repeated the experiment over 10 wt% TiO_2–G for photocatalytic degradation of MB [10 ppm] repetitively for 10 times under UV light (Fig. 7c). The photoactivity of the 10%TiO_2–G was maintained 100% without marked deactivation up to 4 repeated cycles. Then, the photoactivity was slighlty decreases to reach 95% after 10 repeated cycles. The recycle tests demonstrated that TiO_2–G photocatalyst was quite stable during that heterogeneous liquid–solid photocatalytic since slightly decrease in activity was observed even after being used repetitively for 10 times, showing a good potential in photocatalysis applications. The slight decrease indicates that the photocatalytic activity of TiO_2–G nanocomposites has repeatability. The reduction in the degradation efficiency after fourth cycle may be explained by the decrease of the surface for both photon absorption and MB adsorption [46].

To examine visible-light activity, photocatalyst was exposed to halogen lamp. It is worthwhile to mention that commercial TiO_2 P-25 exhibited ~15% photodegradation efficiency toward MB oxidation after 3 h illuminations (Fig. 8a). As seen from Fig. 8a, it provides good photocatalytic activity for MB oxidation over the TiO_2–GO, TiO_2–GN and TiO_2–G. Also, after 2 h irradiation, the total organic carbon (TOC) decreased about 70% in the presence of TiO_2–GO and them complete mineralization of MB after 3 h. The decrease in TOC with the TiO_2–GO photocatalysts is more significant than that with P25 photocatalyst (10%), suggesting the enhanced photodegradation activity under visible light. It is interesting to observe that in this regard, the effective charge transfer can reduce the charge recombination and increase the photocatalytic activity of TiO_2 nanoparticles. Interestingly, electrons in the upper valence band can be directly excited from graphene to the conduction band, that is, the 3d orbitals of TiO_2, under visible light irradiation. This should yield well-separated electron–hole pairs, with potentially high photocatalytic performance in hybrid G and TiO_2 nanocomposites [47]. The positive effect of incorporating GO to enhance the transport of excited electrons from TiO_2 [37]. The visible light response of TiO_2–GO is presumably attributed to the electron transferred from graphene to the CB of TiO_2. Most studies available to date report that enhancements of performances of TiO_2–GO nanocomposites, are mainly attributed to the role of graphene as the electron shuttle to carry excited electrons from the semiconductor rather than sensitizing the semiconductor [17,30,48,49]. This is, therefore, the first to reveal the function of graphene to sensitize TiO_2, while an appropriate interface interaction is achieved in the form of a nanocomposite. Also, the effect of varying the loading (0.1–1 g/l) of the optimum photocatalysts TiO_2–G nanocomposites on MB photodegradation was measured and the results were shown in Fig. 8b. The findings indicate that there is a very sharp increase of MB photodegradation at low loadings of photocatalyst 0.1 g/l and a maximum in production at; 0.1 g/l is similar photodegradation rate at high loading amount 1 g/l. The variation of the loading in a fairly wide range (from 0.1 to 1 g/l) does not alter the MB photodegradation. This seems for two reasons; firstly, when the loading of a suspension is high, the flux of absorbed photons is larger, which generates more •OH radicals, that is, the generation rate of •OH radicals increases. Secondly, at 0.1 g/l of photocatalyst creates electrons which facilities the separation of

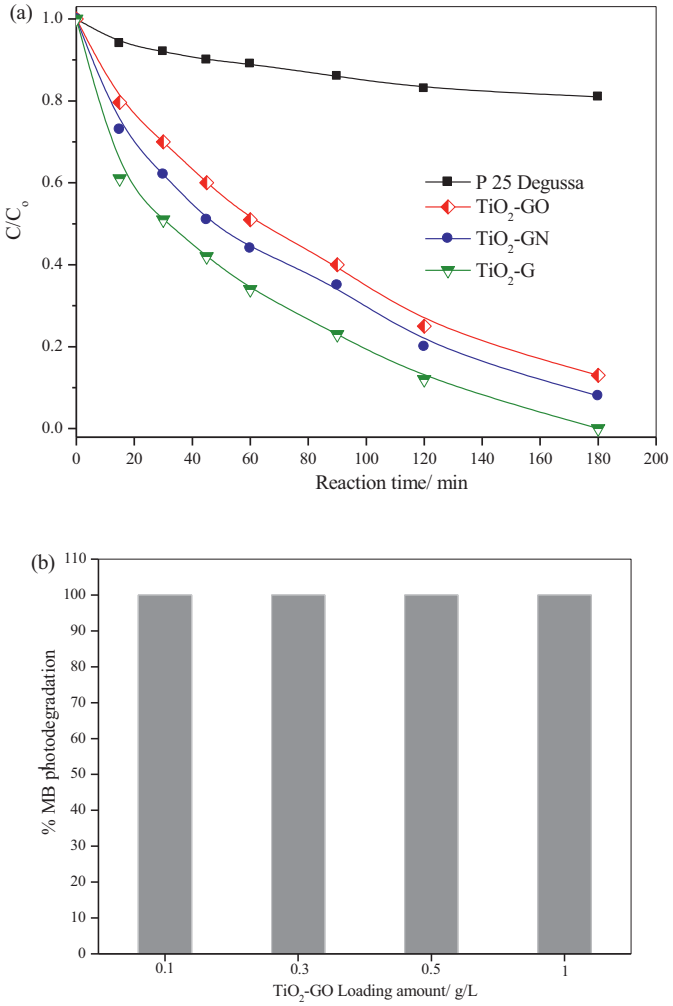

Fig. 8. (a) Photocatalytic degradation of MB in aqueous solution over 10 wt% TiO_2–GO heat treated at 450 °C under inert (N_2)TiO_2–GN, reducing (N_2/H_2) TiO_2–G and oxidizing (O_2) TiO_2–GO samples and Degussa P-25 under visible-light (MB concentration [10 ppm]; (b) photocatalyst loading, 0.5 g/l volume of MB = 100 ml). (b) Effect of TiO_2–G loading at 0.1, 0.3, 0.5 and 1 g/l under visible light.

e^-/h^+ pairs photogenerated. In general, the crystallization of TiO_2 on the surface of G helped to prevent the restacking of graphene sheets and the good distribution of TiO_2 particles and the multilayers structure of G will benefit the photocatalysis and reduce the consumed amount of photocatalysts. Also, the higher conductivity leads to more effective charge separation and more effective antirecombination even at low loadings of photocatalyst 0.1 g/l during photocatalytic process. Consequently, the photocatalytic activity of TiO_2–G have been improved.

4. Conclusions

Facile decoration of graphene oxide (GO) and reduced graphene oxide (G) sheets with TiO_2 nanoparticles at different contents (1–10%) has been demonstrated. The prepared TiO_2–GO were heat treated at 450 °C under oxidizing (O_2), inert (N_2) and (Ar) and reducing (N_2/H_2) conditions. The average crystal size of anatase (1 0 1) is ranged 5–15 nm. The FTIR results confirmed the formation of Ti—O—C bonds between TiO_2 and either GO and G. The photocatalytic efficiency of TiO_2–GO were heat treated at 450 °C under oxidizing (oxygen), inert (N_2) and (argon) and reducing (N_2/H_2) has been enhanced in the order TiO_2–G > TiO_2–GN > TiO_2–GO. The photocatalytic degradation rates of MB by TiO_2–G are faster 6 and 2

times than that by P25 and TiO_2–GO respectively. From the economic point of view, the consumed amount of TiO_2–GO sheets in photocatalysis process is one fifth of commercial P-25 without loss of photocatalytic performance.

Acknowledgments

The authors acknowledge Dr. T. Nunney and R.G. White, Thermo Fisher Scientific, UK for XPS measurements and Hwang S. Woon, Advanced Materials and NanoResearch Centre, Najran University, Saudi Arabia for TEM measurements.

Appendix A. Supplementary data

Supplementary data associated with this article can be found, in the online version, at http://dx.doi.org/10.1016/j.apcatb.2012.09.024.

References

[1] A.K. Geim, K.S. Novoselov, Nature Materials 6 (2007) 183–191.
[2] M. Ishigami, J.H. Chen, W.G. Cullen, M.S. Fuhrer, E.D. Williams, Nano Letters 7 (2007) 1643.
[3] M.J. McAllister, J.L. Li, D.H. Adamson, H.C. Schniepp, A.A. Abdala, J. Liu, M. Herrera-Alonso, D.L. Milius, R. Car, R.K. Prudhomme, I.A. Aksay, Chemistry of Materials 19 (2007) 4396.
[4] R.R. Nair, P. Blake, A.N. Grigorenko, K.S. Novoselov, T.J. Booth, T. Stauber, N.M.R. Peres, A.K. Geim, Science 320 (2008) 1308.
[5] E. Bekyarova, M.E. Itkis, P. Ramesh, C. Berger, M. Sprinkle, W.A. De Heer, R.C. Haddon, Journal of the American Chemical Society 131 (2009) 1336.
[6] G. Williams, B. Seger, P.V. Kamat, ACS Nano 2 (2008) 1487.
[7] P.V. Kamat, Journal of Physical Chemistry Letters 1 (2010) 520–527.
[8] O. Akhavan, ACS Nano 4 (2010) 4174–4180.
[9] O. Akhavan, M. Choobtashani, E. Ghaderi, Journal of Physical Chemistry C 116 (2012) 9653–9659.
[10] W. Qian, R. Hao, Y. Hou, Y. Tian, C. Shen, H. Gao, X. Liang, Nano Res. 2 (2009) 706–712.
[11] O. Akhavan, M. Abdolahad, A. Esfandiar, M. Mohatashamifar, Journal of Physical Chemistry C 114 (2010) 12955–12959.
[12] J. Zhang, Z. Xiong, X.S. Zhao, Journal of Materials Chemistry 21 (2011) 3634.
[13] G. Williams, P.V. Kamat, Langmuir 25 (2009) 13869–13873.
[14] H. Zhang, X. Lv, Y. Li, Y. Wang, J. Li, ACS Nano 4 (2010) 380–386.
[15] O. Akhavan, E. Ghaderi, Journal of Physical Chemistry C 113 (2009) 20214–20220.
[16] S. Sun, L. Gao, Y. Liu, Applied Physics Letters 96 (8) (2010) 083113.
[17] X.Y. Zhang, H.P. Li, X.L. Cui, Y. Lin, Journal of Materials Chemistry 20 (2010) 2801–2806.
[18] Y. Liang, H. Wang, H.S. Casalongue, Z. Chen, H. Dai, Nano Research 3 (2010) 701–705.
[19] Y-H. Ding, P. Zhang, H-M. Ren, Q. Zhuo, Z-M. Yang, Y. Jiang, Materials Research Bulletin 46 (2011) 2403–2407.
[20] Y. Zhou, Q. Bao, L.A.L. Tang, Y. Zhong, K.P. Loh, Chemistry of Materials 21 (2009) 2950–2956.
[21] D-H. Yoo, V. Cuong, V.H. Pham, J.S. Chung, N.T. Khoa, E.J. Kim, S.H. Hahn, Current Applied Physics 11 (2011) 805–808.
[22] Y. Wang, R. Shi, J. Lin, Y. Zhu, Applied Catalysis B 100 (2010) 179–183.
[23] B. Neppolian, A. Bruno, C.L. Bianchi, M. Ashokkumar, Ultrasonics Sonochemistry 19 (2012) 9–15.
[24] J. Liu, H. Bai, Y. Wang, Z. Liu, X. Zhang, D.D. Sun, Advanced Functional Materials 20 (2010) 4175–4181.
[25] J. Liu, L. Liu, H. Bai, Y. Wang, D.D. Sun, Applied Catalysis B 106 (2011) 76–82.
[26] Z.-S. Wu, W. Ren, L. Gao, B. Liu, C. Jiang, H.-M. Cheng, Carbon 47 (2009) 493–499.
[27] C. Gomez-Navarro, R.T. Weitz, A.M. Bittner, M. Scolari, A. Mews, M. Burghard, Nano Letters 7 (2007) 3499–3503.
[28] A.B. Bourlinos, D. Gournis, D. Petridis, T. Szabo, A. Szeri, I. Dekany, Langmuir 19 (2003) 6050.
[29] W.S. Hummers, R.E. Offeman, Journal of the American Chemical Society 80 (1958) 1339.
[30] S. Stankovich, R.D. Piner, X.Q. Chen, N.Q. Wu, S.T. Nguyen, R.S. Ruoff, Journal of Materials Chemistry 16 (2006) 155–158.
[31] K. Zhou, Y. Zhu, X. Yang, X. Jiang, C. Li, New Journal of Chemistry 35 (2011) 353–359.
[32] N.I. Kovtyukhova, P.J. Ollivier, B.R. Martin, T.E. Mallouk, S.A. Chizhik, E.V. Buzaneva, A.D. Gorchinskiy, Chemistry of Materials 11 (1999) 771.
[33] C. Xu, X.D. Wu, J.W. Zhu, X. Wang, Carbon 46 (2008) 386–389.
[34] S. Stankovich, D.A. Dikin, R.D. Piner, K.A. Kohlhaas, A. Kleinhammes, Y. Jia, Y. Wu, S.T. Nguyen, R.S. Ruoff, Carbon 45 (2007) 1558–1565.
[35] J.F. Shen, Y.Z. Hu, C. Li, C. Qin, M. Shi, M.X. Ye, Langmuir 25 (2009) 6122–6128.
[36] S.-K. Joung, T. Amemiya, M. Murabayashi, K. Itoh, Chemistry-A European Journal 12 (2006) 5526.
[37] N. Yang, J. Zhai, D. Wang, Y. Chen, L. Jiang, ACS Nano 4 (2010) 887–894.
[38] S. Stankovich, R.D. Piner, X. Chen, N. Wu, S.T. Nguyen, R.S. Ruoff, Journal of Materials Chemistry 16 (2006) 155.
[39] Y.X. Xu, H. Bai, G.W. Lu, C. Li, G.Q. Shi, Journal of the American Chemical Society 130 (2008) 5856.
[40] S. Sakthive, H. Kisch, Angewandte Chemie International Edition 42 (2003) 4908.
[41] A.A. Ismail, D.W. Bahnemann, L. Robben, V. Yarovyi, M. Wark, Chemistry of Materials 22 (2010) 108–116.
[42] Y.H. Ng, I.V. Lightcap, K. Goodwin, M. Matsumura, P.V. Kamat, Journal of Physical Chemistry Letters 1 (2010) 2222–2227.
[43] R. Czerw, B. Foley, D. Tekleab, A. Rubio, P.M. Ajayan, D.L. Carroll, Physical Review B 66 (2002) 033408.
[44] P.W. Chou, Y.S. Wang, C.C. Lin, Y.J. Chen, C.L. Cheng, M.S. Wong, Surface and Coatings Technology 204 (2009) 834–839.
[45] M.R. Hoffmann, S.T. Martin, W. Choi, D.W. Bahnemann, Chemical Reviews 95 (1995) 69–96.
[46] F. Wang, K. Zhang, Journal of Molecular Catalysis A: Chemical 345 (2011) 101–107.
[47] A. Du, Y.H. Ng, N.J. Bell, Z. Zhu, R. Amal, S.C. Smith, Journal of Physical Chemistry Letters 2 (2011) 894–899.
[48] Y.S. Seo, C. Lee, K.H. Lee, K.B. Yoon, Angewandte Chemie International Edition 44 (2005) 910–913.
[49] Y.H. Ng, A. Iwase, A. Kudo, R. Amal, Journal of Physical Chemistry Letters 1 (2010) 2607–2612.